ACS OMEGA

Open Access

http://pubs.acs.org/journal/acsodf

Article

Zinc Doped Akermanite: A Promising Biomaterial for Orthopedic Application with Enhanced Bioactivity, Mechanical Strength, and Bacterial Study

Shobana Kothandam, Selvatharani V, Naveensubramaniam Vijayakumar, Raveena Ann Alex, Jayanthi Abraham, Selvarasu Maheshwaran, and Sasikumar Swamiappan*

Cite This: *ACS Omega* 2025, 10, 1911−1926

Read Online

ACCESS | Metrics & More | Article Recommendations

ABSTRACT: Incorporating zinc into biocompatible materials has been identified as a potential strategy for promoting bone regeneration and osteogenic activity during hard tissue regeneration. This work aimed to investigate the impact of zinc doping on the structure of akermanite, which was synthesized using the sol−gel combustion method, with the goal of improving the biological response. Powder XRD and FT-IR analysis confirmed the phase purity and the respective functional groups associated with Zn-doped akermanite. Further XPS analysis confirmed the presence of zinc with the respective binding energies in the akermanite matrix. According to the results obtained from the analysis, the apatite-forming ability of Zn-doped akermanite demonstrated enhanced apatite deposition on the surface of the pellet after 9 days of immersion in the SBF medium. The measured mechanical parameters, including compressive strength (140−189 MPa) and Young's modulus (2505−3599 MPa), fall within the range of human cortical bone. Antimicrobial results showed an improved inhibition rate of the doped ceramics compared to pure akermanite with an inhibition percentage of 87% even at lower concentrations. The hemocompatibility of the materials showed hemolysis of human blood cells within the acceptable range without exhibiting toxicity. Cytotoxicity results demonstrate the biocompatibility of the materials with the MG-63 cell line. Based on the results, akermanite doped with zinc at optimal concentrations was found to be compatible and nontoxic promoting it as a potential alternative for bone regeneration in orthopedic applications.

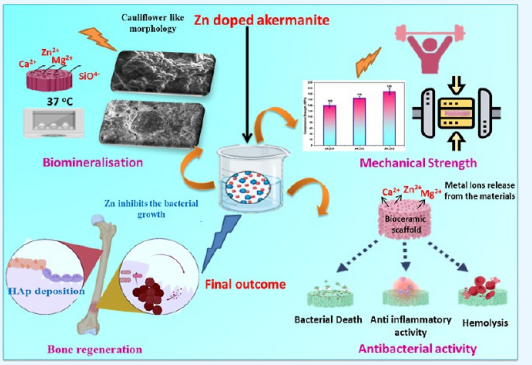

1. INTRODUCTION

Bone is a dynamic tissue with distinctive architecture and features enable it to continuously remodel and acclimatize to the metabolic and mechanical demands of the body, ensuring vitality, mobility, and stability throughout every stage.[1] Thus, replacing natural bone in cases of fracture or bone disease is challenging in tissue engineering.[2] To overcome these challenges, biomaterials have been created to anchor implants in bone, and are considered a remarkable life-saving advancement in materials chemistry. To substitute bone, the synthesized material should possess a porous nature, surface roughness, biocompatibility, suitable mechanical strength and better interaction between bone cells and the substituted material.[3] Bioactive materials containing silicon demonstrate exceptional capacity to activate bone-related genes, drive cell growth, and produce bone-like hydroxyapatite forming ability both in vitro and in vivo.[4] Calcium silicate bioceramics exhibit excellent osteoconductivity that is comparable to conventional calcium phosphate and play a crucial role as a cross-linking agent in connective tissue helping in collagen type 1 formation and bone healing.[5] Additionally, they increase bioactivity and promotes osteoblast development and bone mineralization. Magnesium (Mg) is an essential component of the human body because it aids in the stabilization of DNA, the development of the skeleton, and bone metabolism. Magnesium ions have a similar effect on insulin (a recognized growth factor for osteoblasts), significantly increasing osteoblast adhesion and stimulating osteoblast proliferation.[6] Bioceramics actively contribute to the formation of an apatite-like structure on the surface of damaged tissues through their bone-bonding compounds, which establish chemically stable contact with the surrounding tissues.[7] By influencing the chemical composition of physiological fluids, these materials stimulate the development of apatite when

Received: June 12, 2024
Revised: December 4, 2024
Accepted: December 6, 2024
Published: January 10, 2025

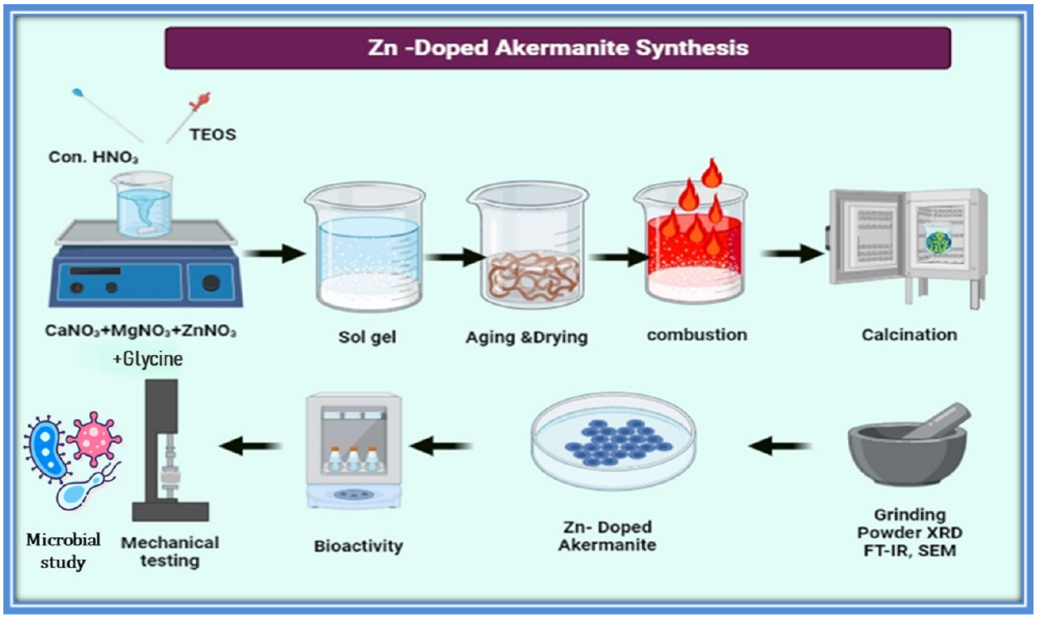

Figure 1. Schematic representation for the preparation of Zn doped akermanite.

come into contact with the appropriate aqueous medium.[8] New generations of bioceramics have been developed due to their capacity to promote bone regeneration that resembles the natural biological tissues of the human body. For optimal bone regeneration, it is important that the rate of degradation matches the pace at which host bone tissues regenerate after implantation owing to chemical dissolution and cell-mediated disintegration.[9] The introduction of new materials into the body may lead to infection, making the prevention of infectious diseases a significant challenge. Selective dopants typically present in bone tissue may be added to regulate dissolution processes.[10] A multitude of therapeutic ions, such as copper (Cu), strontium (Sr), and silver (Ag), are used in the field of biomaterials to enhance biological properties, including promoting the growth of new blood vessels (angiogenesis), influencing bone growth (osteogenesis), and inhibiting bacterial progression. Silicate ceramics have been suggested as viable materials that may exhibit antibacterial properties and improve bone growth due to their beneficial structure and composition.[11−13] Zinc is an essential element in several enzymes in the human body and its role as a dopant in bioactive ceramics influences the material's ability to combat infections while promoting bone regeneration.[14] It can enhance DNA synthesis and enzyme activity, and possesses antibacterial properties similar to those of copper ions.[15] Therefore, a deficiency of this ion is linked to reduced bone density due to its ability to inhibit the formation of bone resorbing cells (osteoclasts) while promoting the function of bone-building cells (osteoblasts).[16] As zinc deficiency reduces bone mass and slows bone metabolism, it has received particular attention in tissue regeneration.[17] The replacement of Zn^{2+} in the HA lattice has been extensively investigated in recent decades due to its essential role in the metabolic processes of bone formation. Based on previous literature, the maximum amount of zinc that can be substituted in the HA lattice is found to be in the range of 15−25% mol.[18−20] However, the extent of substitution is influenced by the preparation conditions. Minimal inclusion of zinc in the hydroxyapatite lattice actively promotes cell proliferation and differentiation;[21] however, cytotoxicity has been observed at significant concentrations of zinc in the matrix of the parent material (>1.2 wt %).[22] Zn-substituted HA has also been thoroughly explored for its ability to inhibit the growth of bacteria and fungi after implantation.[23] Furthermore, the lattice constant of Zn-substituted HA decreases progressively as Zn insertion increases, primarily because the Zn^{2+} ion has a smaller ionic radius (0.74 Å) compared to that of Ca^{2+} (1.00 Å). However, the lattice constant does not exhibit a consistent trend and instead fluctuates as the dopant content increases.[16] According to the findings, akermanite shows strong in vitro bioactivity and can be employed as biodegradable fillers in the body.[24] Modifications in material composition can aid in fine-tuning the biological characteristics of the parent material with enhanced activities.[25] The sol−gel combustion route was utilized to synthesize the material; this strategy is well-known for being conventional and energy-efficient compared to other synthesis techniques.[26] Previous research has demonstrated that Zn-HAp, synthesized via the sol−gel spin coating technique, exhibited enhanced antibacterial properties against the pathogens *Staphylococcus aureus* and *C. albicans* compared to pure HAp.[27] Similarly, Nigam et al., and Pawar et al., reported that antibacterial assays using zinc-doped magnesium ferrite demonstrated strong suppression of *Escherichia coli*.[28] In a recent investigation conducted by Neščáková et al., zinc-doped bioactive glass was prepared using a micro emulsion-assisted sol−gel process. Additionally, Zn-BG showed no cytotoxic effects on embryonic fibroblasts and osteoblast-like cells, promoting the proliferation of these cells. Furthermore, Zn-BG exhibited enhanced protein adsorption compared to undoped BG.[29] In a previous study conducted by Bigham et al., it was found that the addition of zinc-doped magnesium silicate to a composite scaffold made of polycaprolactone (PCL) and silk fibroin (SF) resulted in improved cell adhesion and alkaline phosphatase (ALP) activity compared to the pure material.[30] Tridoped Ag/Mg/Zn-HAp samples demonstrated lower cytotoxicity (IC_{50} value of 53.184) and greater biocompatibility (IC_{50} value of 58.068) than pure HAp in an earlier investigation on the L929 cell line.[31] In light of the

https://doi.org/10.1021/acsomega.4c05482
ACS Omega 2025, 10, 1911−1926

preceding literature this study presents the synthesis of zinc-doped akermanite using a sol−gel combustion approach. A thorough investigation was conducted to examine the purity of the Zn-akermanite phase and its structural morphology. The impact of Zn^{2+} doping on apatite formation ability, mechanical strength, antibacterial properties, hemolytic activity and cytotoxicity was examined and discussed.

2. EXPERIMENTAL METHOD

2.1. Synthesis of Zinc-Doped Akermanite. Tetraethyl orthosilicate (Acros Organics, 98%), magnesium nitrate hexahydrate (98%, SD fine), calcium nitrate tetrahydrate (98%, SD fine), zinc nitrate (99.0%, Qualigens), glycine (99.5%, SD fine AR), and concentrated nitric acid were employed in the synthesis of Zn-doped akermanite through the sol−gel combustion method. The appropriate amounts of calcium, magnesium and zinc nitrates were first added to a beaker along with glycine as fuel. Following the addition of TEOS, concentrated nitric acid was then added resulting in the hydrolysis of TEOS. The mixture was stirred continuously for 2 h at room temperature to obtain a dense gel. After the dense gel matrix formed, it was left to aging for 24 h at room temperature. The gel obtained was dried at 150 °C in an oven for 2 days. It was then combusted in a muffle furnace at 400 °C and calcined at temperature of 900 °C to obtain Zn-doped akermanite as the final material.[32,33] The calcined powders were labeled as AK-Zn1, AK-Zn2 and AK-Zn3 corresponding to the amount of zinc incorporated in akermanite. Figure 1 represents the schematic representation of the synthesis of Zn-doped akermanite. The compositions of the samples are presented in Table 1.

Table 1. Composition of AK-Zn1, AK-Zn2 and AK-Zn3

sample code	Zn composition (M)	Zn doped akermanite $Ca_{2-X}Zn_XMgSi_2O_7$
AK-Zn1	0.03	$Ca_{0.97}Zn_{0.03}MgSi_2O_7$
AK-Zn2	0.06	$Ca_{0.94}Zn_{0.06}MgSi_2O_7$
AK-Zn3	0.09	$Ca_{0.91}Zn_{0.09}MgSi_2O_7$

2.2. Pellets Preparation. The pellets were prepared using a hydrolytic press machine according to ASTM standards. The powders were finely ground and pressed into pellets under a load of 5 tons, resulting in pellets with a diameter of 12 mm and a thickness of 6 mm. The pellets were utilized for in vitro studies.

2.3. Characterization Techniques. The phase analysis of the calcined samples was performed using an AD8 Advanced Powder X-ray Diffractometer (Bruker AXS GmbH, Karlsruhe, Germany), employing a Cu/Kα radiation filter at a wavelength of 1.5406 Å. FTIR spectra were recorded using a Shimadzu IR Affinity-1 CE FTIR Spectrophotometer across a range of 400 to 4000 cm^{-1} to analyze the respective functional groups. The structural morphology and elemental composition were analyzed using an EVO18 Research SEM (Zeiss India) equipped with an energy-dispersive X-ray analysis unit functioning at 30 kV. A 200 kV FEI-Tecnai G2 20 S-TWIN high-resolution transmission electron microscope was utilized to analyze the morphology and perform selected area of electron diffraction. The assessment of mechanical properties was carried out using a universal testing machine (UTM) INSTRON 8801, featuring a load weight accuracy of ±0.5%. XPS data were analyzed using a thermal ESCALAB 11,250 system equipped with a monochromatic Al Kα X-ray source (1486.6 eV).

2.4. Porosity Measurement. The porosity of Zn-doped akermanite bioceramics was determined using the liquid displacement method based on Archimedes principle.[34] First, the dry pellet was weighed in air to obtain the weight ($W1$). The sample was then suspended in absolute ethanol, ensuring complete submersion, and allowed to saturate for approximately 24, 48, and 72 h. While submerged, the weight of the sample was recorded as ($W2$). Afterward, the sample was carefully removed, excess liquid was drained, and the weight while suspended in ethanol was noted as ($W3$). The porosity was calculated using the formula is shown in eq 1

$$\text{porosity} = \frac{W2 - W1}{W2 - W3} \times 100\% \quad (1)$$

2.5. Antifungal and Antibacterial Activity. The antifungal activity of zinc-doped akermanite AK-Zn1, AK-Zn2, and AK-Zn3 was evaluated using *Aspergillus niger* (*A. niger*) and *Fusarium oxysporum* (*F. oxysporum*). The antifungal efficacy of the akermanite powder was determined using the broth dilution method. In 100 mL of potato dextrose broth, 500 μL of the clinical pathogens was added to a 250 mL of Erlenmeyer flask with different concentrations of the ceramic powders (0.5, 1, and 2 mg/mL). The flasks were incubated for 48 h at 37 °C and filtered through Whatman filter paper to determine the dry weight of the fungus. The percentage of dry weight inhibition against the fungal pathogens was calculated with and without the (eq 2) ceramic powders (control) using the following formula

$$\text{percentage of dry weight (\%)} = \frac{\text{dry weight of the control} - \text{dry weight of the test}}{\text{Dry weight of the control}} \times 100 \quad (2)$$

The antibacterial activities of zinc-doped akermanite bioceramics, (AK-Zn1, AK-Zn2, and AK-Zn3) were assessed against four clinical pathogens, *Staphylococcus aureus* (*S. aureus*), *Staphylococcus epidermidis* (*S. epidermidis*), *Escherichia coli* (*E. coli*), and *Pseudomonas aeruginosa* (*P. aeruginosa*) using the broth dilution technique. The zinc-doped akermanite samples consisted of overnight bacterial cultures and added to flasks containing Luria−Bertani medium consisting of bacterial suspensions and ceramic powders at concentrations of 0.5, 1 and 2 mg/mL. The flasks were incubated for 24 h, and bacterial growth inhibition was assessed by measuring the optical absorbance at 600 nm. The percentage inhibition of pathogenic bacteria by zinc-doped akermanite powder was calculated by comparing the optical density of the control sample (without the ceramic powder) with that of the test sample. The formula used to calculate the percentage (eq 3) of inhibition is[34]

$$\text{percentage of inhibition (\%)} = \frac{CF - BCF}{CF} \times 100 \quad (3)$$

were, BCF-final concentration (200 μL) of the zinc-doped akermanite powder with an organism. CF-control broth with the test clinical pathogens.

To check the colony formation 100 μL of the control and broth media with the ceramic powders was examined in Luria−Bertani medium. The test was conducted in triplicate and the

https://doi.org/10.1021/acsomega.4c05482
ACS Omega 2025, 10, 1911−1926

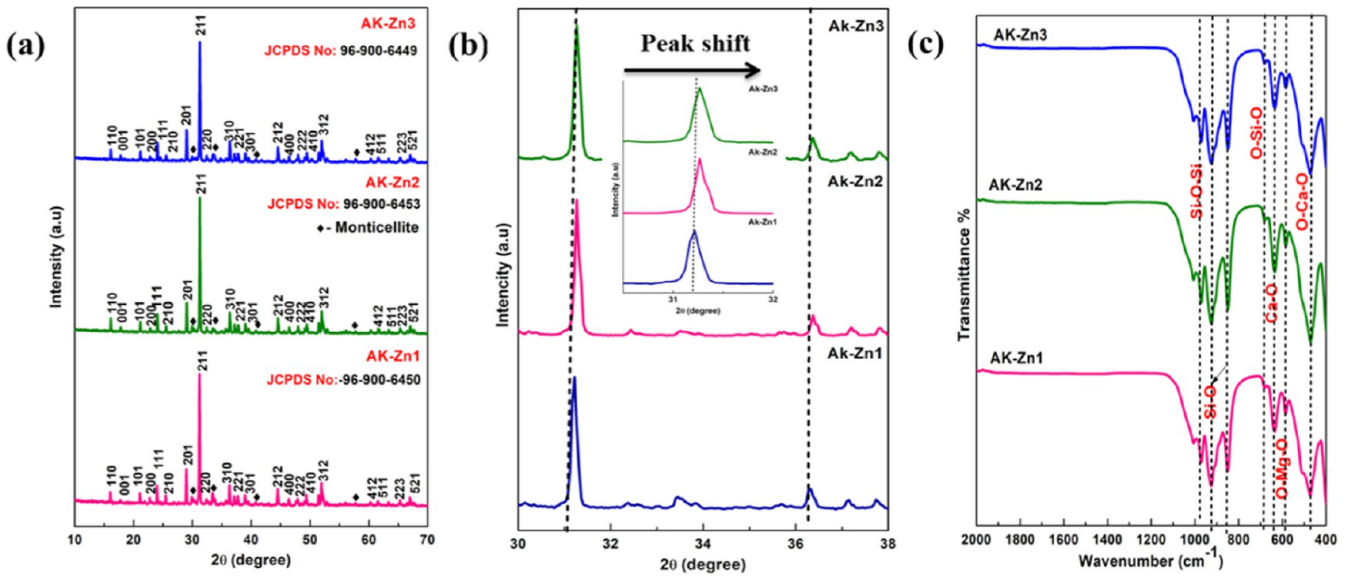

Figure 2. (a) XRD pattern (b) peak shift and (c) FT-IR spectrum of AK-Zn1, AK-Zn2, and AK-Zn3.

results are represented as mean and standard deviation. The interaction between the zinc-doped akermanite and the clinical pathogens were observed using a scanning electron microscope (Zeiss Evo 18)

2.6. Anti-inflammatory Activity. The anti-inflammatory activity of human red blood cells was evaluated using the HRBC membrane stabilization method.[35] Blood samples were collected from healthy individuals. For the test, the reaction mixture consisted of 1 mL of zinc- doped akermanite solution (AK-Zn1, AK-Zn2, and AK-Zn3) at different concentrations (0.5, 1, 2 mg/mL) and 10% RBC suspension. Diclofenac was used as the positive control. The formula used to determine the percentage of inhibition is as follows (eq 4)

$$\text{percentage of inhibition} = \frac{(\text{absorbance of control} - \text{absorbance of sample})}{\text{absorbance of control}} \times 100 \quad (4)$$

2.7. Hemolysis Assay. A hemolysis assay was performed on a blood sample (5 mL) obtained from a healthy volunteer using EDTA as an anticoagulant, according to protocol.[35] After isolating red blood cells (RBCs) through centrifugation at 1000 rpm for 5 min and washing them three times with PBS, the blood-PBS mixture was diluted with 9 mL of PBS. For the hemolysis assay, 250 μL of the diluted blood with PBS solution was mixed with zinc-doped akermanite powder at various concentrations ranging from 0.5 to 2 mg/mL. The absorbance was measured at 545 nm after incubation for 1 h incubation at 37 °C. The formula used to calculate the hemolytic percentage is given in eq 5

$$\text{HR \%} = \frac{\text{Dt} - \text{Dnc}}{\text{Dpc} - \text{Dnc}} \times 100 \quad (5)$$

where Dt = akermanite powder's absorbance. Dnc = the absorbance of the negative control (10 mL PBS with 0.2 mL diluted blood). Dpc = the absorbance of the positive control (10 mL distilled water with 0.2 mL diluted blood)

2.8. MTT Assay. The MG-63 bone cancer cell line was obtained from the National Centre for Cell Science (NCCS), Pune. The cells were cultured in Eagle's Minimum Essential Medium (EMEM) supplemented with 10% fetal bovine serum (FBS). The cultures were maintained at 37 °C in a 5% CO_2 atmosphere, with 95% air and 100% relative humidity. Maintenance cultures were passaged weekly, and the culture medium was replaced twice a week. Monolayer cells were detached using trypsin-ethylene diamine tetraacetic acid (EDTA) to create single-cell suspensions. Viable cells were counted using a hemocytometer and diluted in medium containing 5% FBS to achieve a final cell density of 1×10^5 cells/mL. A 100 μL aliquot of the cell suspension was seeded into each well of a 96-well plate at a plating density of 10,000 cells per well and incubated to allow cell attachment at 37 °C, 5% CO_2, 95% air, and 100% relative humidity. After 24 h, the cells were treated with serial dilutions of the test samples. The samples were initially dissolved in neat dimethyl sulfoxide (DMSO), and an aliquot of this solution was diluted with serum-free medium to achieve twice the desired final maximum test concentration. Four additional serial dilutions were prepared to provide a total of five sample concentrations. Aliquots of 100 μL from each dilution were added to the wells containing 100 μL of medium, achieving the final sample concentrations. The plates were incubated for an additional 48 h at 37 °C, 5% CO_2, 95% air, and 100% relative humidity. Wells containing medium without samples served as controls, and all concentrations were tested in triplicate. 3-(4,5-Dimethylthiazol-2-yl)-2,5-diphenyltetrazolium bromide (MTT) is a yellow, water-soluble tetrazolium salt. In living cells, the mitochondrial enzyme succinate dehydrogenase cleaves the tetrazolium ring, converting MTT to an insoluble purple formazan product. The amount of formazan produced is directly proportional to the number of viable cells. After 48 h of incubation, 15 μL of MTT solution (5 mg/mL in phosphate-buffered saline, PBS) was added to each well and incubated at 37 °C for 4 h. The medium containing MTT was then discarded, and the formazan crystals were dissolved in 100 μL of DMSO. The absorbance was measured at 570 nm using a microplate reader.[36]

2.9. Statistical Analysis. Statistical analysis was performed using a one-way ANOVA test, with a significance level of $p < 0.05$. All experimental groups were evaluated in triplicate.

https://doi.org/10.1021/acsomega.4c05482
ACS Omega 2025, 10, 1911−1926

3. RESULTS AND DISCUSSION

3.1. Phase Analysis Study. The XRD pattern and FT-IR spectrum of zinc-doped akermanite samples (AK-Zn1, AK-Zn2, and AK-Zn3) are shown in Figure 2. The diffracted patterns of zinc-doped akermanite show a small shift in lattice parameter characteristics without affecting the tetragonal structure of the parent material. The peak shift arises from slight modifications in the material caused by the doping process, which involves the incorporation of foreign atoms (Zn^{2+}) into the crystal lattice (Ca^{2+}) of akermanite. The peak shift toward the higher angle might be due to the smaller ionic radii of the dopant Zn^{2+} (0.74 Å) compared to the parent atom Ca^{2+} (1.00 Å).[37−39] This causes the alteration in the lattice parameter values, as indicated in the table. JCPDS card no.: 96-900-6450, 96-900-6453 matches with AK-Zn1, AK-Zn2. JCPDS card no.: 96-900-6449 matches with AK-Zn3. There was a notable appearance of peaks at 2θ = 16°, 24°, 29°, 31°, 36°, 44°, 49° and 52°. The average crystallite size (D) of the zinc-doped akermanite samples was determined using (eq 6) Scherrer's formula depicted in Table 2.

Table 2. Lattice Parameter and Crystalline Size Values

sample code	lattice parameter (Å)		crystal system	avg. crystalline size (nm)
	$a = b$	c		
AK-Zn1	7.8338	5.0082	tetragonal	39−43
AK-Zn2	7.8154	4.9719	tetragonal	37−40
AK-Zn3	7.8037	4.9696	tetragonal	31−34

$$D = \frac{K\lambda}{\beta \cos\theta} \tag{6}$$

where β is the full-width half-maximum, k is the Scherrer constant, D is the crystallite size, and λ is the wavelength of X-ray.

In Figure 2 O−Ca−O stretching mode is indicated by the band with the highest intensity at 472 cm^{-1}. The O−Mg−O vibrational modes of akermanite were linked to the band at 586 cm^{-1}. The vibrational band corresponding to Ca═O group was observed at 636 cm^{-1}. The Si−O stretching modes are shown by the peaks at 852 and 935 cm^{-1}. The symmetric stretching vibration of Si−O−Si was ascribed to the peak observed at 1024 cm^{-1}.[36] Figure 3 shows that SEM observations confirmed the presence of a cluster-like agglomerated morphology resulting from the high temperature calcination, and the corresponding elemental compositions of Ca, Mg, Si, O and Zn were detected, as validated by the EDX

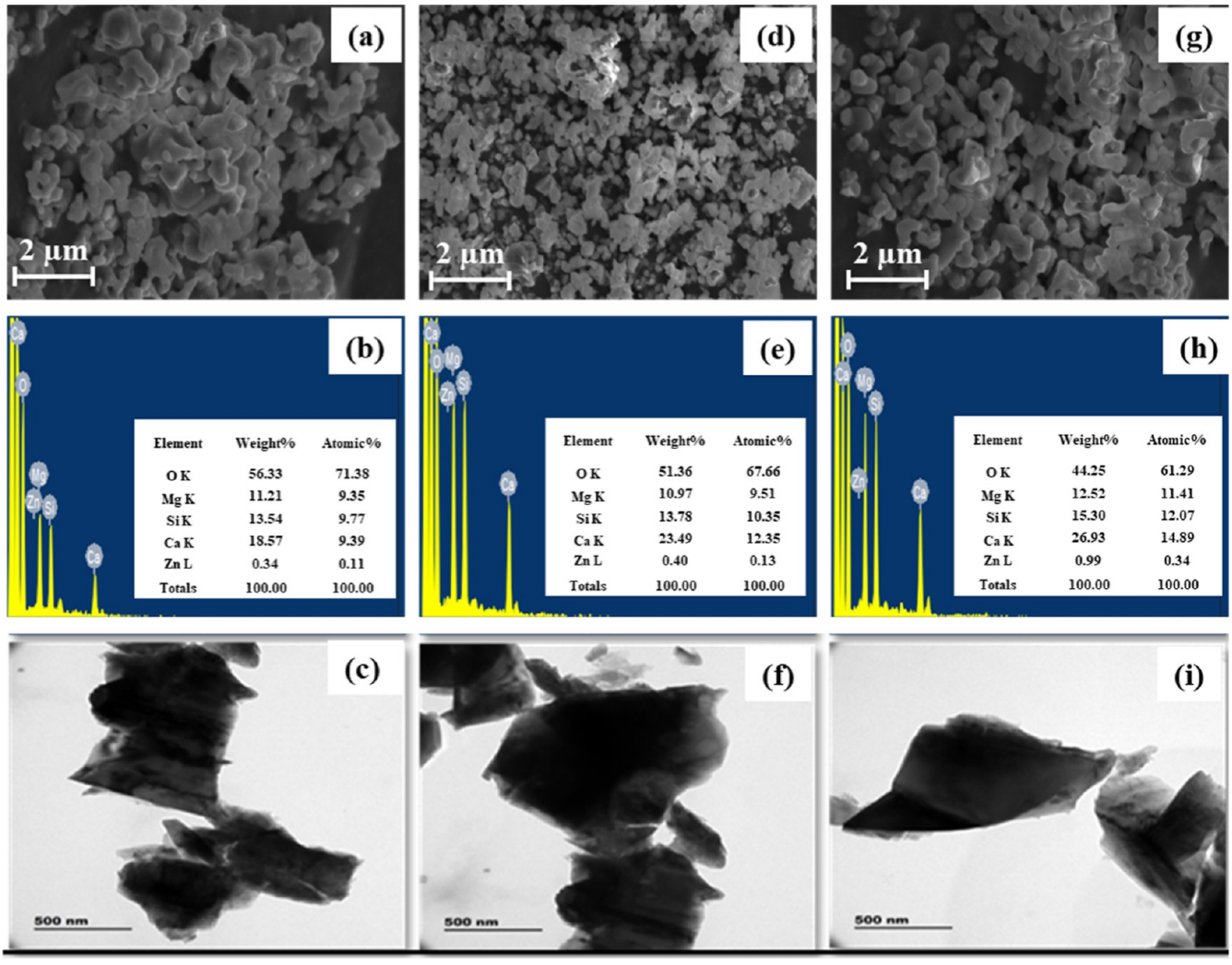

Figure 3. SEM/EDX, TEM micrograph of zinc doped akermanite AK-Zn1 (a−c), AK-Zn2 (d−f), AK-Zn3 (g−i).

https://doi.org/10.1021/acsomega.4c05482
ACS Omega 2025, 10, 1911−1926

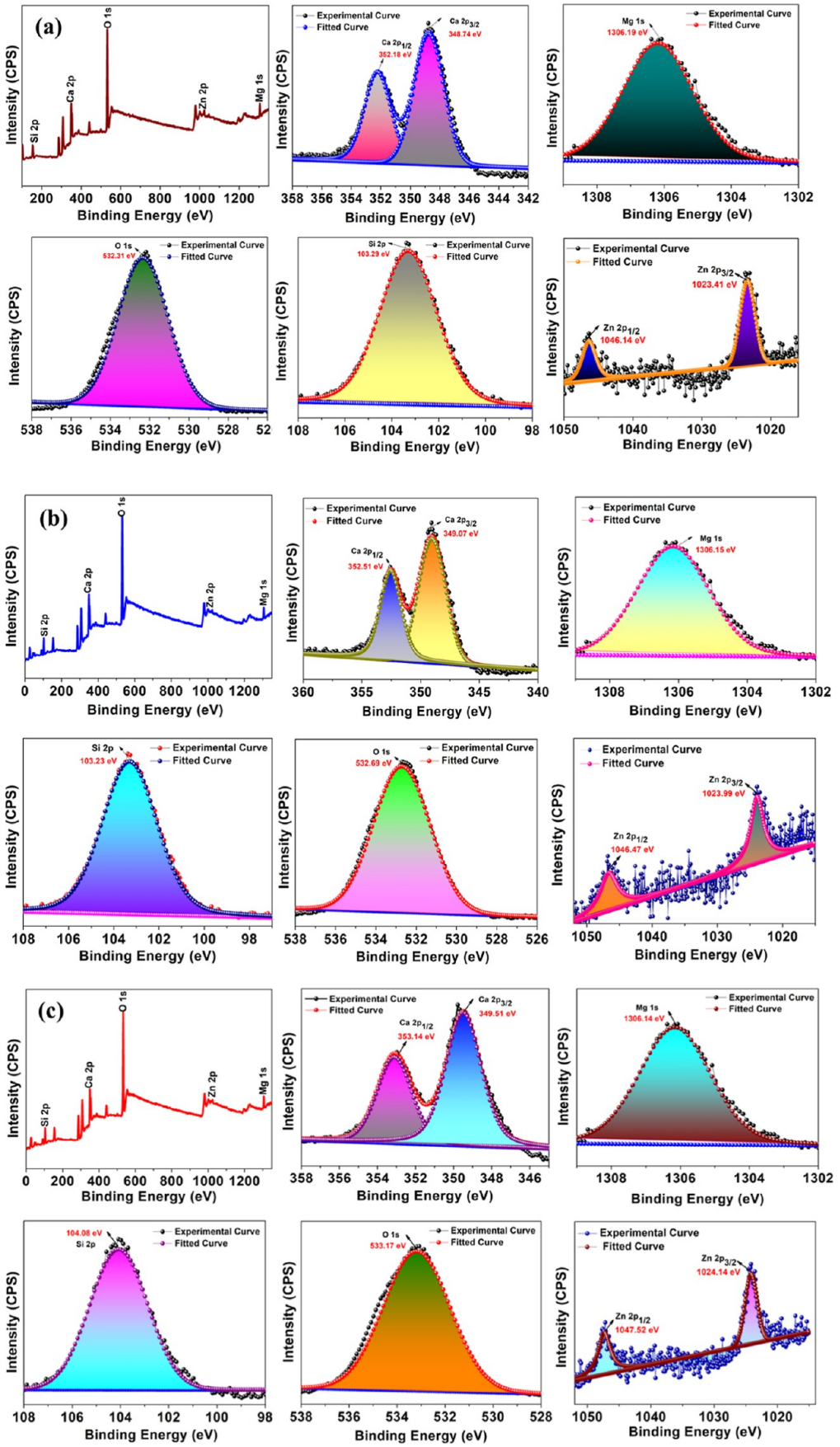

Figure 4. XPS spectrum of zinc doped akermanite (a) AK-Zn1, (b) AK-Zn2, (c) AK-Zn3.

https://doi.org/10.1021/acsomega.4c05482
ACS Omega 2025, 10, 1911−1926

Table 3. Elemental Composition of AK-Zn1, AK-Zn2 and AK-Zn3 from the XPS Analysis

elemental composition	AK-Zn1	AK-Zn2	AK-Zn3
Ca 2p	14.1	13.56	14.45
Mg 1s	4.89	4.9	6.04
Si 2p	20.65	20.25	19.52
O 1s	59.34	60.08	58.22
Zn 2p	1.03	1.22	1.77

spectrum. Subsequent TEM investigations revealed the polycrystalline nature of the prepared doped materials.[40]

3.2. XPS Analysis. The elemental composition and oxidation states of zinc-doped akermanite were determined through XPS analysis. Electron emission occurs from the sample once it absorbs sufficient energy, resulting in kinetic energy. An electron detector quantifies the energy of the emitted electrons and generates a graphical display of their energies and the corresponding electron frequencies. Figure 4 displays the comprehensive XPS spectra of the zinc-doped akermanite indicating the presence of calcium, magnesium, oxygen, silicon, and zinc. Figure 4a–c show detailed analysis of the Ca 2p, O 1s, Mg 1s, Si 2p, and Zn 2p orbital states using high-resolution deconvolution techniques. The deconvoluted Ca 2p spectra exhibited two distinct binding energy peaks at 348.74–353.14 eV, corresponding to the Ca $2p_{1/2}$ and Ca $2p_{3/2}$ states, respectively. The deconvoluted O 1s spectra exhibit a single prominent peak at a binding energy of 532.31–533.17 eV. Similarly, the Mg 1s spectra exhibited a significant peak with a binding energy of 1306.14–1306.19 eV. The Si 2p spectrum exhibits a single peak between 103.29 and 104.08 eV. The deconvoluted Zn spectra exhibit two intense binding energy peaks in the range of 1023.41–1046.47 eV, identified as the energy states of the Zn $2p_{3/2}$ and Zn $2p_{1/2}$ orbitals, respectively. Elemental composition of AK-Zn1, AK-Zn2 and AK-Zn3 from the XPS analysis is depicted in Table 3. XPS analysis revealed the presence of zinc in the calcium site of the akermanite bioceramic.[41,42]

3.3. In Vitro Bioactivity Assay. To assess the bioactivity of the synthesized zinc-doped akermanite, the samples were made into pellets and exposed to the stimulated body fluid (SBF) solution for 3, 6, and 9 days at a temperature of 37 °C. Calcined powders of zinc-doped akermanite were formed into pellets with a diameter of 12 mm and height of 6 mm. For 9 days, the pellets (AK-Zn1, AK-Zn2, and AK-Zn3) were submerged in 50 mL of SBF in a covered conical flask. The samples were incubated at 37 °C undisturbed and the SBF was changed every 24 h. At specific time intervals, the pellets were separated from the solution, cleaned using distilled water, and allowed to dry at 60 °C in a hot air oven for 3 h. Hydroxyapatite deposition on the surface of the pellets was characterized using X-ray diffraction techniques (XRD). When

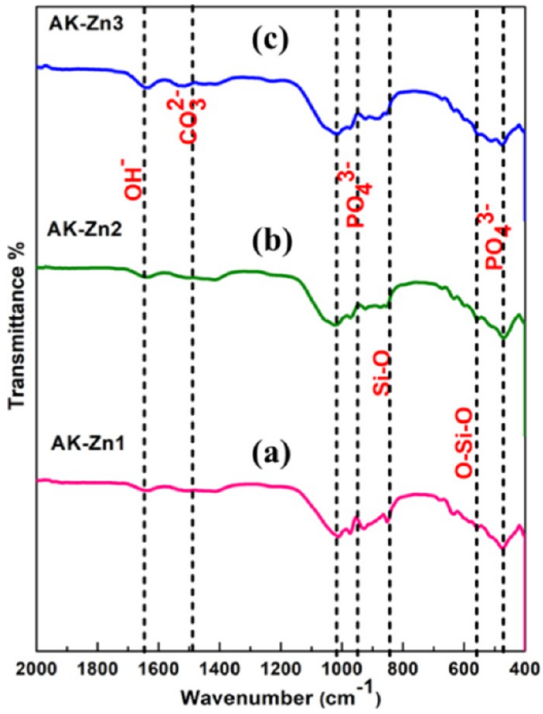

Figure 6. FT-IR spectrum of (a) AK-Zn1, (b) AK-Zn2, (c) AK-Zn3 immersed in SBF after 9 days.

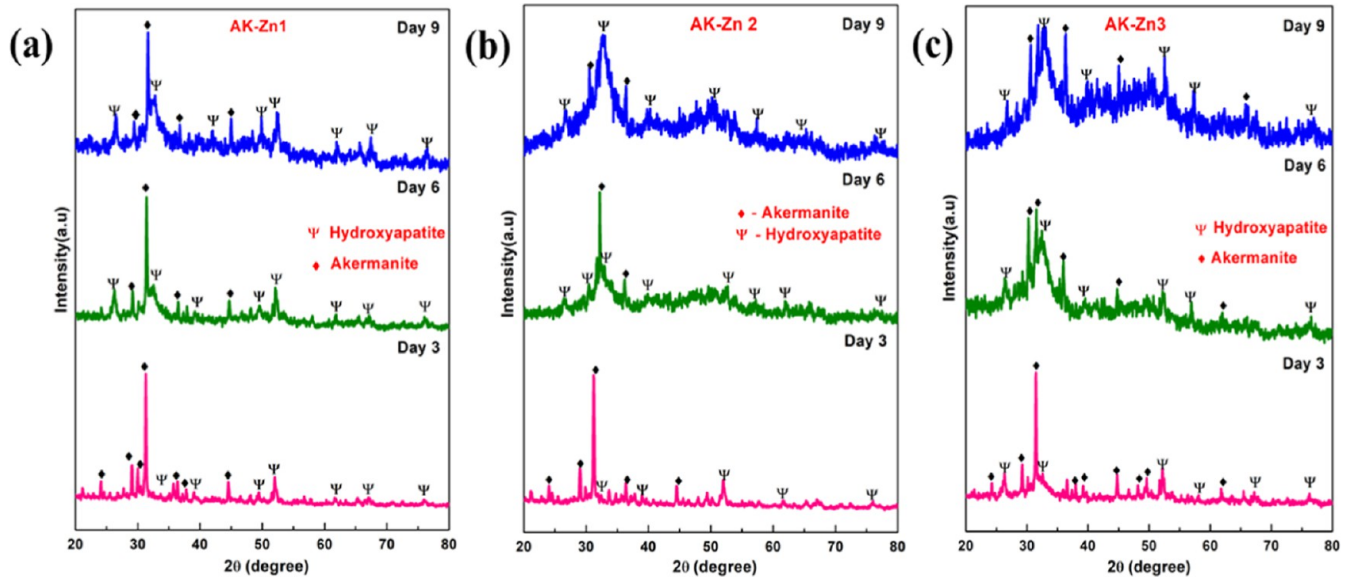

Figure 5. XRD pattern of (a) AK-Zn1, (b) AK-Zn2, (c) AK-Zn3 immersed in SBF after 9 days.

https://doi.org/10.1021/acsomega.4c05482
ACS Omega 2025, 10, 1911–1926

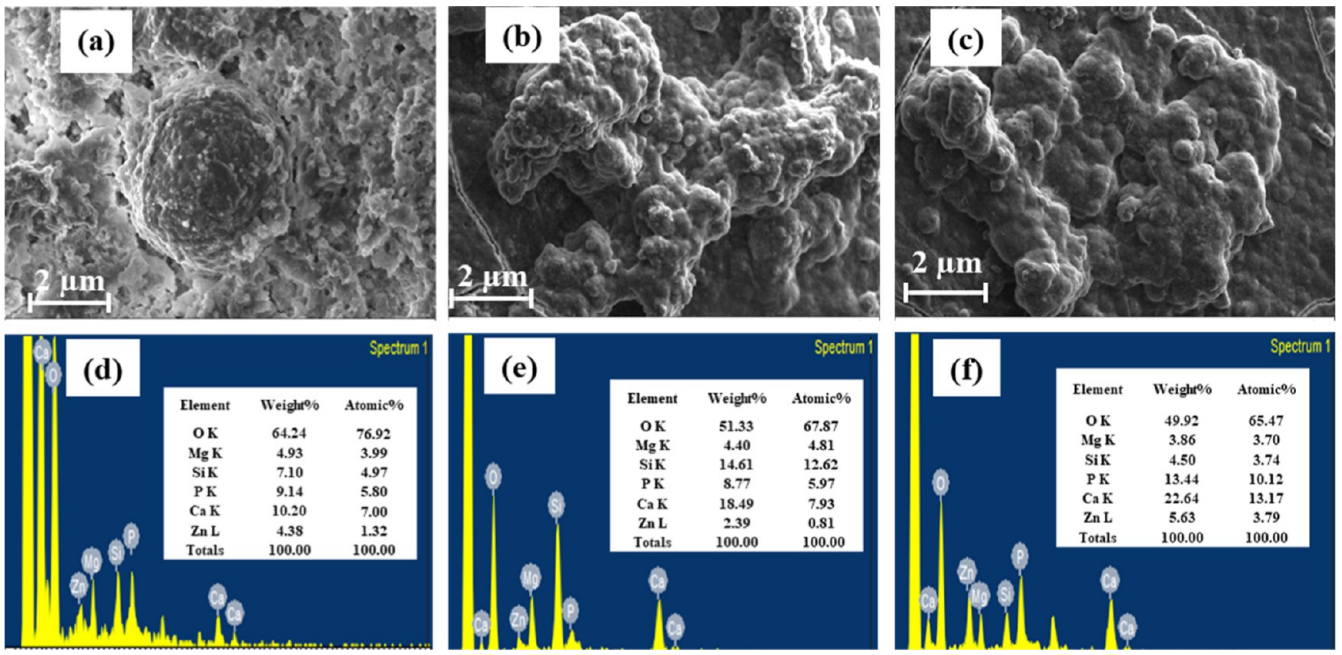

Figure 7. SEM (a–c) /EDX (d–f) of AK-Zn1, AK-Zn2, AK-Zn3 immersed in SBF after 9 days.

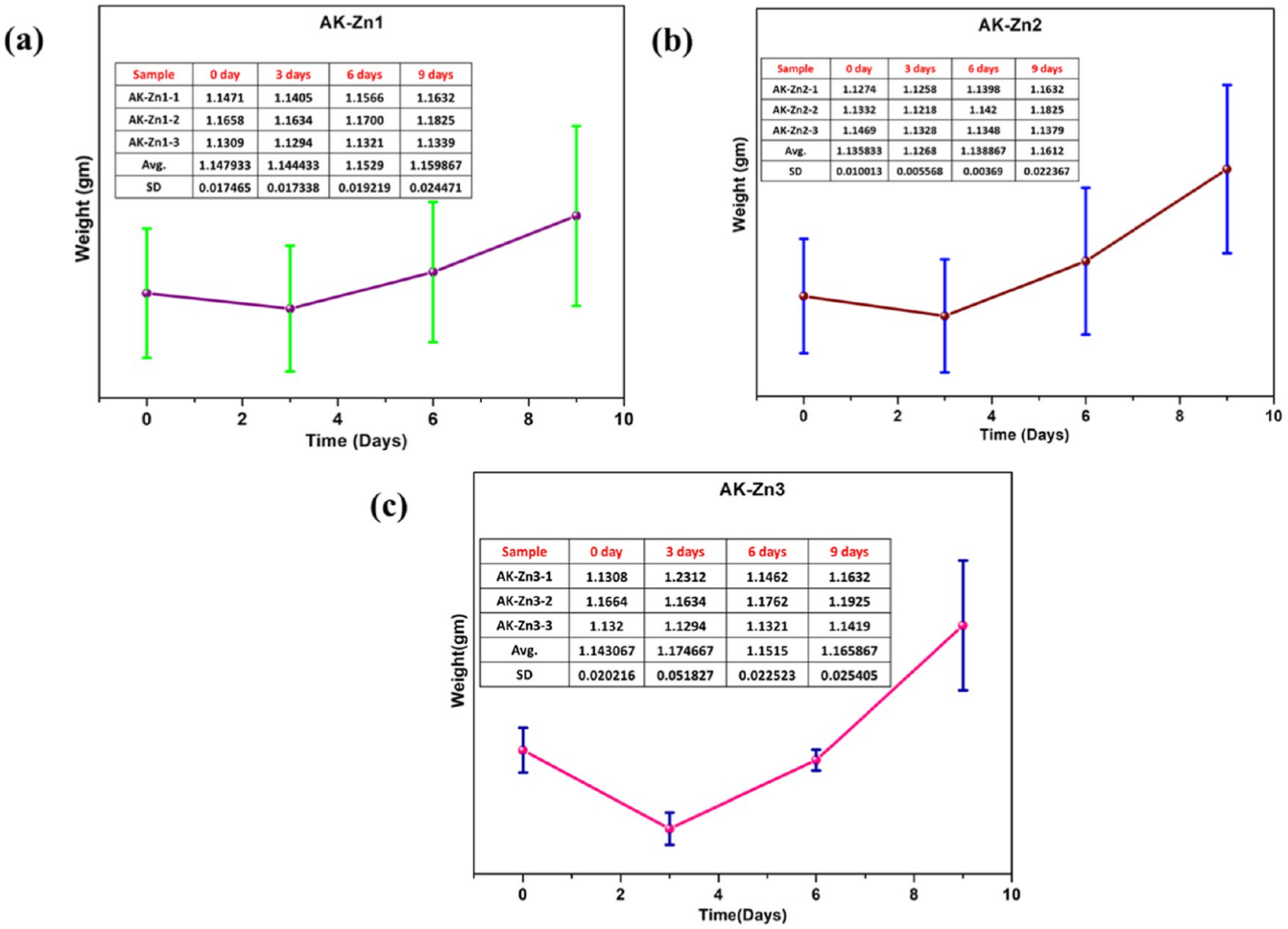

Figure 8. Degradation plot of zinc doped akermanite scaffolds immersed in SBF medium (a) AK-Zn1, (b) AK-Zn2 and (c) AK-Zn3 ($p > 0.05$ is considered statistically not significant).

Zn^{2+} ions act as network formers, the network connectivity increases due to the formation of Zn–O–Zn and Si–O–Zn linkages.[43] The incorporation of Zn^{2+} ions with Ca^{2+} ions as network modifiers in the akermanite structure, reinforces the

https://doi.org/10.1021/acsomega.4c05482
ACS Omega 2025, 10, 1911–1926

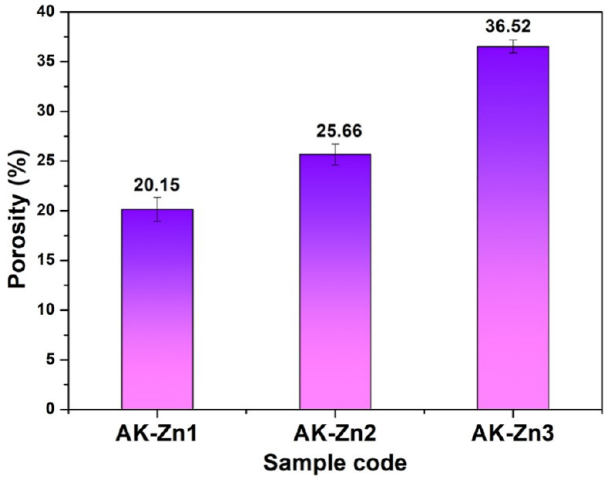

Figure 9. Porosity measurement s of AK-Zn1, AK-Zn2 and AK-Zn3.

structure, as ionic radii of Zn^{2+} are smaller than those of Ca^{2+}. Consequently, the release of ions is decreases in the initial stages.[44] The XRD pattern reveals that after 6 days of immersion, a higher zinc concentration enhances hydroxyapatite (HAp) deposition, attributed to the formation of additional active sites due to smaller crystal size and higher porosity, which subsequently promotes biomineralization.[45]

According to the XRD data in Figure 5 apatite formation in akermanite with Zn^{2+} is more intense than in pure akermanite ceramic. To investigate the impact of zinc ion concentration on apatite production, all three scaffolds were immersed in SBF for 9 days. Due to Zn^{+2} partial doping in the Ca^{2+} site during hydrolysis, the calcium and oxygen interactions weaken, aiding formation of hydroxyapatite layer on the surface of the pellets. The development of an apatite layer on the akermanite surfaces varied significantly among AK-Zn1, AK-Zn2, and AK-Zn3 despite the same soaking duration. This difference was attributed to variable ion leaching from zinc-doped akermanite. Crystalline HAp peaks developed, but the akermanite peaks did not entirely disappear. Compared to the other two compositions, AK-Zn3 exhibited highest bioactivity. The development of apatite crystals in the akermanite system was accelerated by Zn-doping into the calcium sites, during the short immersion period. The formation of apatite layer on the surface of the implants is crucial for direct bone- implant attachment. The effect of metal ions on bioactivity was further confirmed by FT-IR analysis, as shown in Figure 6. After 9 days of immersion, the peaks of the Zn-akermanite decreased, while new phosphate peaks of hydroxyapatite formed on the surface of the pellets. The Ca−O and O−Mg−O peaks steadily decreased due to the growth of phosphate deposition, whereas the strength of the substrate Si−O peaks gradually diminished. This indicates that calcium and magnesium were hydrolyzed during the initial phase of the biomineralization process.[45,46] Typical bending, and stretching modes of vibrational bands at 1030−1090, 574 , and 471 cm^{-1} were observed in the FT-IR spectra. At 1462 cm^{-1}, the bending modes CO_3^{2-} groups were identified. The OH^- bending vibrational frequency was noted at 1646 cm^{-1}. In the Zn^{2+} doped bioceramics, there was a significant increase in apatite formation.[47] The intensity of the phosphate peak steadily increased after 9 days of immersion, while the intensity of the substrate peaks gradually decreased. Complete coverage of hydroxyapatite crystals on the pellets surface was achieved after 9 days of immersion.

Table 4. Mechanical Properties of Different Types of Bone and Zn Doped Akermanite

types of bone/material	compressive strength (MPa)	young's modulus (GPa)
cortical bone	130−200	7−30
cancellous bone	0.1−16	0.05−0.5
AK-Zn1	140	2.50
AK-Zn2	166	3.45
AK-Zn3	189	3.59

The formation of a HAp layer on the surfaces of AK-Zn1, AK-Zn2 and AK-Zn3 pellets after soaking in SBF was further confirmed by SEM and energy dispersive X-ray spectroscopy (EDX) analysis. Figure 7 depicts the development of spherical and cauliflower-like morphologies on the surface of the zinc-doped akermanite. This morphology is a distinctive characteristic of apatite crystals formed during biomineralization.[48] AK-Zn2 and AK-Zn3 pellets exhibited a greater number and larger size of granules on their surface compared to AK-Zn1, indicating variations in morphology. This trend could be attributed to the reduced particle size of the samples, which facilitated the development of larger apatite deposits. The EDX

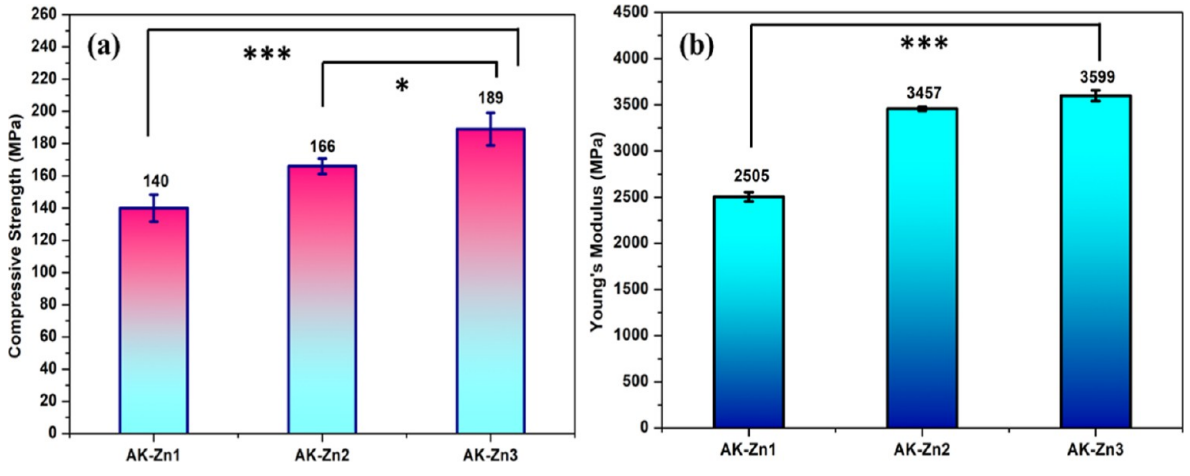

Figure 10. (a) Compressive strength and (b) Young's modulus of immersed in SBF after 9 days (*$p < 0.05$, ***$p < 0.001$ is considered statistically significant).

https://doi.org/10.1021/acsomega.4c05482
ACS Omega 2025, 10, 1911−1926

Table 5. Percentage of Inhibition of Zinc Doped Akermanite Powders AK-Zn1, AK-Zn2 and AK-Zn3 against Clinical Pathogens

sample	*E.coli* %	P.aeruginosa %	S.aureus %	S.epidermidis %
AK-Zn1 (0.5 mg/mL)	28.15	35.75	42.10	25.24
AK-Zn1 (1 mg/mL)	40.21	45.32	57.21	38.35
AK-Zn1 (2 mg/mL)	72.30	58.12	69.10	57.21
AK-Zn 2 (0.5 mg/mL)	20.91	19.31	56.12	52.10
AK-Zn 2 (1 mg/mL)	52.71	45.32	68.53	68.27
AK-Zn 2 (2 mg/mL)	80.31	67.10	76.70	78.31
AK-Zn3 (0.5 mg/mL)	57.21	24.15	40.30	35.70
AK-Zn3 (1 mg/mL)	65.32	32.61	67.17	59.20
AK-Zn3(2 mg/mL)	85.10	64.20	87.22	79.13

Table 6. After Incubation for 24 h, the Change in pH of Clinical Pathogens

sample		E.coli	P.aeruginosa	*S.epidermidis*	S.aureus
control		6.8	6.8	6.8	6.8
AK-Zn1	0.5 mg/mL	7.0	7.1	7.1	7.2
	1 mg/mL	7.0	7.1	7.2	7.1
	2 mg/mL	7.1	7.1	7.1	7.2
AK-Zn 2	0.5 mg/mL	7.0	7.0	7.3	7.0
	1 mg/mL	7.2	7.1	7.1	7.3
	2 mg/mL	7.2	7.2	7.1	7.1
AK-Zn3	0.5 mg/mL	7.0	7.1	7.2	7.2
	1 mg/mL	7.1	7.1	7.3	7.2
	2 mg/mL	7.2	7.2	7.2	7.3

Table 7. Dry Weight of Different Ceramic Powders AK-Zn1, AK-Zn2 and AK-Zn3 against Fungal Pathogens

sample	F. oxysporum (%)	A. niger (%)
AK-Zn1	45.4	54.5
	51.4	64.2
	60.5	77.5
AK-Zn2	65.3	60.2
	74.6	65.5
	75.1	72.6
AK-Zn3	45.5	40.3
	54.4	67.5
	70.1	78.3

examination showed Ca/P ratios of 1.6, 1.77, and 1.73 for the surface layers of AK-Zn1, AK-Zn2, and AK-Zn3, respectively. These results are closer to the Ca/P ratio of 1.67 seen in natural bone, which mimics HAp.[49] These observations indicate that zinc-doped akermanite has improved bioactivity and can effectively bind to natural bone tissue.

3.4. Degradation Test. Figure 8 depicts the degradation characteristics of zinc doped akermanite. The degradation graph shows the comprehensive fluctuations in weight of the constructed scaffolds during a 9 day immersion in SBF medium. Initially, the scaffolds experience weight loss due to the exchange of weakly bound calcium and zinc ions with hydrogen ions in the SBF medium leading to the formation of a silanol interface. According to the apatite-formation mechanism during immersion in SBF, the ceramics undergo breakdown, resulting in the release of Ca^{2+} and Zn^{2+} ions.[50] These ions are swiftly replaced by H_3O^+ ions present in the SBF. Figure 8 demonstrates that the release of Zn^{2+} ions from akermanite significantly increased. Following the precipitation of a silica-rich layer, the carbonated apatite layer was formed through the incorporation of OH^- and CO_3^{2-} and the attraction of Ca^{2+} and PO_4^{3-} ions from SBF solution. After 3 days, the AK-Zn3 sample displays considerable weight loss, likely due to its elevated Zn^{2+} concentration, which may be loosely packed crystal structure and accelerates early stage degradation. Over time, hydroxyapatite begins to form on the surface, gradually filling voids. This continuous HAp deposition helps counteract material loss and improves the doped ceramic's structural integrity and mechanical strength over extended immersion. The degradation rate of the doped akermanite varied among different samples, with AK-Zn1 showing the slowest degradation, followed by AK-Zn2 and then AK-Zn3. These outcomes are dependent on the concentration of the dopant ions. Based on the findings, it appears that the addition of Zn^{2+} to akermanite positively impacts its degradation, with the extent of the effect being concentration dependent.[51]

3.5. Measurement of Porosity (%). Figure 9 illustrates the porosity measurements of zinc-doped bioceramic pellets. The increase in porosity from 20% to 36% in zinc-doped akermanite bioceramics, as determined by the liquid displacement method, underscores the substantial impact of zinc doping on the material's microstructure. This increase in porosity is likely attributed to zinc ions influencing the crystallization process, which facilitates enhanced pore formation and interconnectivity. Such a significant increase in porosity is crucial for enhancing bioactivity, as it promotes improved nutrient transport, cell adhesion, and proliferation, making zinc-doped akermanite more suitable for bone tissue engineering applications. These findings align with previous literature,[52] which indicates that the incorporation of bioactive ions like zinc can significantly alter the physical properties of bioceramics, thereby enhancing their applicability in biomedical contexts.

3.6. Mechanical Strength Investigation. Figure 10 shows the compressive strength and Young's modulus of the Zn-doped akermanite samples. All three samples were formed into pellets (6 mm in height and 12 mm in width) following ASTM standards using a hydraulic press, and then sintered for 3 h at 500 °C to assess their mechanical properties. After sintering the pellets were allowed to cool to ambient temperature, before being immersed in SBF medium for a period of 9 days. After this immersion the AK-Zn3 sample exhibited highest mechanical strength compared to AK-Zn1, and AK-Zn2. Zinc doping enhances the mechanical strength of akermanite by doping Zn^{2+} ions at Ca^{2+} sites, introducing minor lattice distortions that improve load bearing capacity through localized stress distribution. While porosity generally reduces mechanical strength by lowering material density and structural integrity, optimizing porosity can balance mechanical

https://doi.org/10.1021/acsomega.4c05482
ACS Omega 2025, 10, 1911−1926

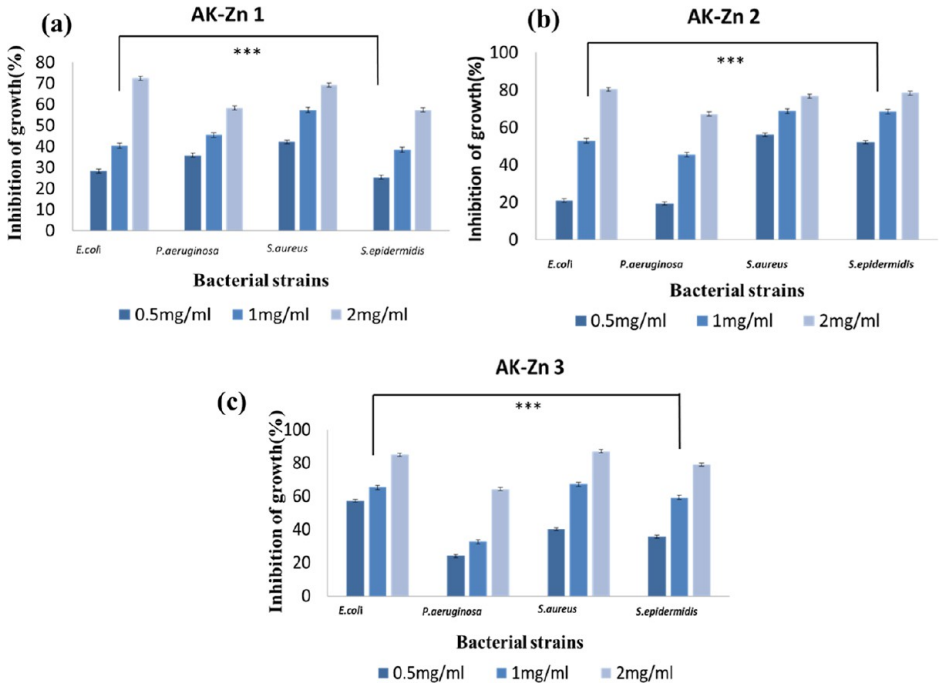

Figure 11. Comparative percentage inhibition of different zinc doped akermanite powders (a) AK-Zn1 (b) AK-Zn2 and (c) AK-Zn3 against clinical pathogens. (***$p < 0.001$ is considered statistically significant).

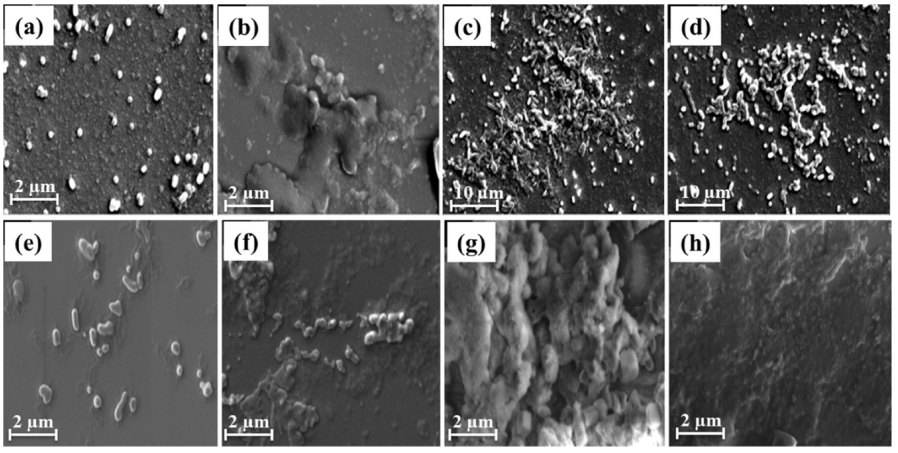

Figure 12. SEM images of (a) *S.aureus* control (b) AK-Zn1(c) AK-Zn2 and (d) AK-Zn3 (e) *E. coli* control (f) AK-Zn1 (g) AK-Zn2 and (h) AK-Zn3 at a concentration of 2 mg/mL.

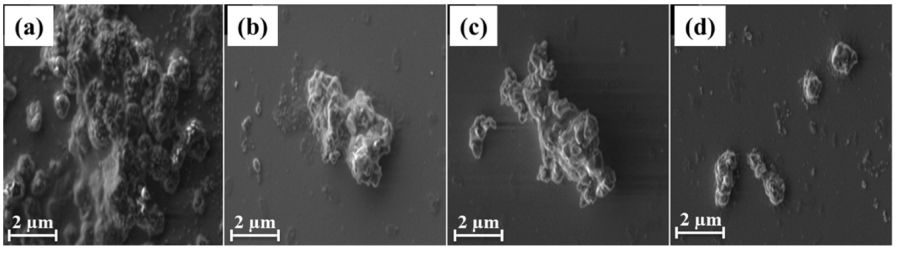

Figure 13. SEM images of (a) *Aspergillus* control (b) AK-Zn1 (c) AK-Zn2 and (d) AK-Zn3 at a concentration of 2 mg/mL.

stability with increased bioactivity. Immersion in simulated body fluid promotes hydroxyapatite deposition on the bioceramic surface, filling pores with HAp crystals. This HAp layer reinforces the scaffold through mineral interlocking, offsetting initial strength losses due to porosity and ultimately contributing to enhanced mechanical stability. The increase in porosity of the Zn-doped akermanite bioceramics, ranging from 20% to 36%, (AK-Zn1 to AK-Zn3) significantly enhanced biomineralisation by facilitating ion supply.[49] Table 4, compares the mechanical strength values with those of human cortical bone. The compressive strength and Young's modulus of AK-Zn3 is 189 MPa, which is significantly higher

https://doi.org/10.1021/acsomega.4c05482
ACS Omega 2025, 10, 1911−1926

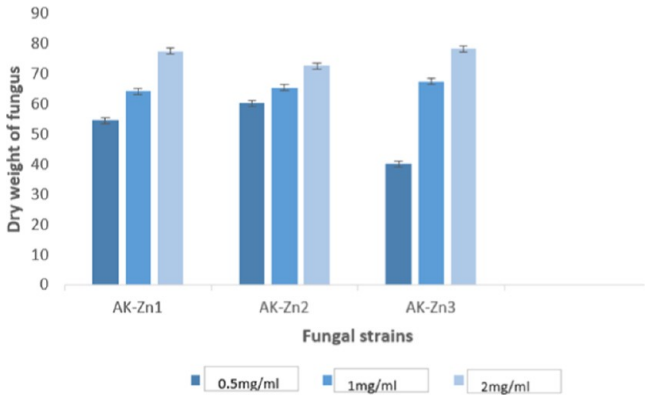

Figure 14. Dry weight of akermanite powders AK-Zn1, AK-Zn2, and AK-Zn3 against *A. niger* (control).

than those of other AK-Zn1, AK-Zn2, exhibiting a nearly 1.4 times higher. Similar outcomes are observed for the young's modulus as well 3599 MPa. The mechanical characteristics of ceramic bodies are influenced by various factors, including the dopant, particle size and HAp deposition process.[48]

3.7. Antibacterial and Anti-fungal Activity. Studies have shown that zinc ions can inhibit various bacterial activities including glycolysis, acid tolerance, and transmembrane proton translocation.[53,54] Zinc oxide ions exhibit antibacterial effects on both Gram negative bacteria (*E. coli*) and Gram positive bacteria (*S. aureus*) due to a significant increase in oxidative stress. *S. aureus* and *S. epidermidis* were responsible for two of every three isolates. *S. aureus* and *S. epidermidis* serve as the primary causal agents in orthopedic implants, and play a pivotal role in causing two major forms of bone infections, osteomyelitis and septic arthritis, both of which lead to inflammatory deterioration of bones and joints. Osteomyelitis characterized by infection and inflammation within the bone, is primarily caused by *S. aureus, S. epidermidis, P. aeruginosa,* and *E. coli*. The initial and crucial stage of implant infection is bacterial adherence, a complex process influenced by the presence of serum or tissue proteins, bacterial characteristics, material surface features, and environmental factors.[55]

Zinc ions possess strong antibacterial and antifungal properties, with antibacterial effects arising from three aspects: interaction with bacteria, release of zinc ions, and production of reactive oxygen species (ROS). Teichoic acid and lipoteichoic acid are two negatively charged components of bacterial cell walls, which cause the bacteria to have negative charges on their surfaces, whereas zinc ions have a positive charge. Zinc ions and bacteria are attracted to each other by electrostatic forces, which cause Zn^{2+} to accumulate on the surface of the bacteria. This accumulation alters the zeta potential of bacteria and disrupts potassium channels on bacterial cell membranes, which ultimately results in an increase in lipid peroxidation and enhanced membrane permeability. This membrane dysfunction facilitates internalization, leading to excessive intracellular zinc ion accumulation and metabolic changes. Additionally, Zn^{2+} plays a crucial role in antibacterial properties by binding to functional proteins and modifying cell membrane permeability. As the intracellular concentration rises, its interaction with enzyme thiol groups strengthens, impacting bacterial enzymatic reactions, weakening glycolysis, and ultimately inducing cell death.[56] The results obtained from the broth dilution method of bacteria are represented in Table 5, and the fungal sample results are shown in Table 7. Table 5 confirms that AK-Zn3 has a pronounced inhibitory effect with high inhibition percentages of 87.22% for *S. aureus* and 85.10% for *E. coli* compared to the other two ceramic powders, AK-Zn1 and AK-Zn2 (Figure 11). Table 6 displays the effect of pH after 24 h of incubation on clinical pathogens. Zinc doped akermanite powders AK-Zn2 and AK-Zn3 exhibit notable efficacy against potent antibacterial agents and especially effective against Gram-positive bacteria *S. aureus* and Gram-negative bacteria *E. coli*. Table 7 presents the comparative antifungal activities of the ceramic powders against *F. oxysporum* and *A. niger*. The dry weight of akermanite powders of *A. niger* demonstrated more antifungal activity than *F. oxysporum* (Figure 14). These antibacterial and antifungal studies highlight the potential of zinc doped akermanite powders against the tested clinical pathogens and their possible orthopedic applications.

SEM images revealed clustering of pathogenic bacterial and fungal strains both within and around the zinc akermanite powder particles. The SEM images of control strains of *S. auerus* and *E. coli* (Figure 12a–h) showed a smooth surface, whereas the postexperiment test strains, *S. auerus* and *E. coli* treated with ceramic powders, displayed distinct surface alterations. Figure 13 shows the SEM images *Aspergillus* control and ceramic powders treated with the *Aspergillus* strain.

3.8. Hemolysis Assay. Hemolysis of zinc-doped akermanite has not been extensively studied. Given zinc's therapeutic properties and biocompatibility, this trace element was examined in akermanite bioceramic powders for potential applications in medical implants. Hemolysis testing is a critical metric for determining the biocompatibility of synthetic materials with blood, essential for assessing their suitability as implant material in the body. Various factors, such as the concentration of released ions and material degradation products, must be evaluated when considering the hemolytic effects of biomaterials.[57] It can even alter its properties including its degradation characteristics and ion release properties. Red blood cells are highly sensitive to changes in

Table 9. Percentage of Anti-inflammatory HRBC Assay on Different Zn Doped Ceramic Powders

concentration in mg/mL	% inhibition of ceramic powder AK-Zn1	% inhibition of ceramic powder AK-Zn2	% inhibition of ceramic powder AK-Zn3	control drug (diclofenac)
0.5	92.3	91.3	93.1	98.02%
1	94.2	93.7	95.3	
2	96.5	95.3	97.2	

Table 8. Percentage of Hemolysis Assay on Zn Doped Ceramic Powders

concentration in mg/mL	% hemolysis of ceramic powder AK-Zn1	% hemolysis of ceramic powder AK-Zn2	% hemolysis of ceramic powder AK-Zn3	positive control drug (diclofenac)	negative control
0.5	1.9	1.8	2.3	0.98%	0.046%
1	3.7	3.2	4.5		
2	2.3	2.6	3.4		

https://doi.org/10.1021/acsomega.4c05482
ACS Omega 2025, 10, 1911−1926

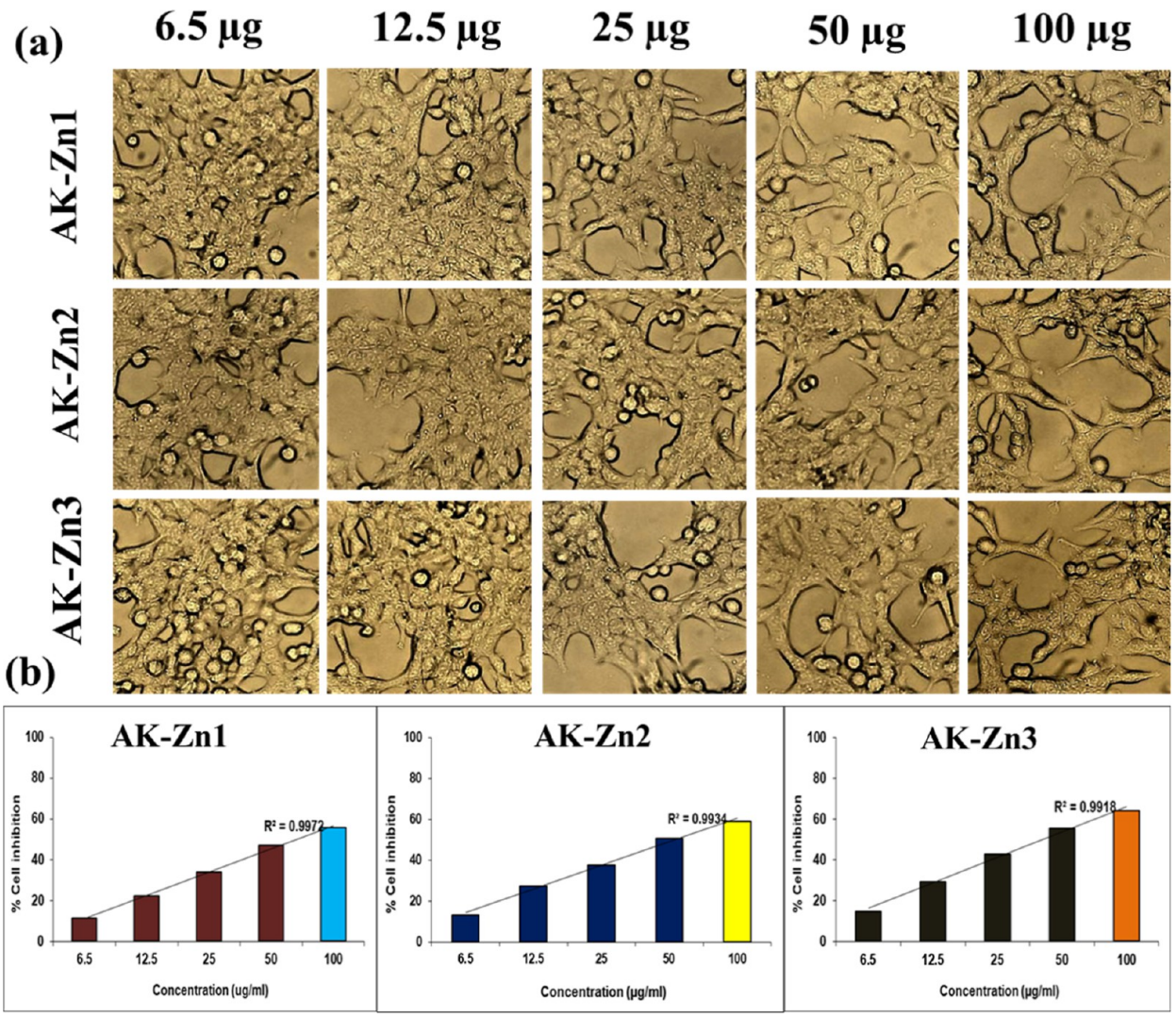

Figure 15. Cytotoxicity effect of AK-Zn1, AK-Zn2 and AK-Zn3. (a) Phase-contrast images, (b) half maximal inhibitory concentration (IC_{50}).

the osmotic environment, and high concentrations of these ions can affect the integrity of cells. Zinc is considered safe for implant studies; excessive release of zinc ions or high concentrations in the bloodstream could potentially lead to hemolysis.[58] The release of zinc ions from doped akermanite is a critical factor. Table 8 shows that up to 2 mg/mL akermanite powder can be used and should not exceed this concentration. The optimum concentration was 1 mg/mL. Here $p < 0.05$ is considered statistically significant for the AK-Zn1, AK-Zn2, and AK-Zn3 samples.

3.9. Anti-inflammatory Study. Zinc is an essential element involved in regulating of inflammatory responses and immune functions. Studies have reported that zinc exerts anti-inflammatory effects by modulating cytokine production and immune cell function.[59] Upon doping akermanite powders with zinc, the release of zinc ions from the doped material over time can contribute to anti-inflammatory effects, and the controlled release of these ions may modulate inflammation at the cellular level. This process indirectly promotes an anti-inflammatory environment during healing. Zinc ions can also impact the production and activity of cytokines, which are signaling molecules involved in immune responses. Zinc may contribute to the regulation of inflammation near the implant site by modulating the cytokine levels. Additionally the antioxidant property of zinc helps neutralize reactive oxygen species (ROS), which can cause inflammation and tissue damage. By reducing oxidative stress zinc can mitigate inflammation near the implant site,[60] creating more favorable microenvironment for bone cells to adhere to and grow around the implant. Table 9 displays the percentage of anti-inflammatory activity in doped ceramic powders compared to the control. According to the results AK-Zn3 demonstrated 97.2% efficiency at a concentration of 2 mg/mL, which is close to the control drug level. For the AK-Zn1 sample, a $p > 0.05$ is considered statistically nonsignificant, while for the AK-Zn2 and AK-Zn3 samples, $p < 0.05$ is considered statistically significant.

3.10. Cytotoxicity. The in vitro cytotoxicity of Zn-doped akermanite bioceramics (AK-Zn1, AK-Zn2, AK-Zn3) in MG-63 cells was evaluated, showing IC_{50} values of 59.41, 48.47, and 38.26 μg/mL, respectively. AK-Zn3 exhibited the highest cytotoxicity with 63.94% inhibition, followed by AK-Zn2 (58.89%) and AK-Zn1 (55.62%). These results indicate a dose-dependent cytotoxic effect, with higher Zn concentrations leading to greater inhibition of cell proliferation in the MG63 cell line. This outcome is consistent with previous findings in metal ion-doped bioceramics, where higher dopant levelsare associated with increased cytotoxicity.[61] This underscores the

https://doi.org/10.1021/acsomega.4c05482
ACS Omega 2025, 10, 1911−1926

importance of optimizing Zn ion concentration to ensure biocompatibility for tissue regeneration applications. Figure 15 illustrates the cytotoxic effects of AK-Zn1, AK-Zn2, and AK-Zn3: (a) phase-contrast images and (b) IC_{50} values.[62]

4. CONCLUSION

The addition of zinc to akermanite presents a promising approach for developing biomaterials specifically tailored for orthopedic applications. Zinc-doped akermanite was successfully synthesized using the sol−gel combustion technique with three distinct zinc concentrations (0.03, 0.06, and 0.09 M). The emergence of pure phase was confirmed by analyzing the X-ray diffraction (XRD) patterns of AK-Zn1, AK-Zn2 and AK-Zn3 are accomplished at a temperature of 900 °C. X-ray photoelectron spectroscopy (XPS) analysis verified the presence of a dopant within the akermanite crystal lattice. Following bioactivity testing, the surface of the pellet exhibited a cauliflower-like shape, implying the deposition of hydroxyapatite with AK-Zn3 showed a higher level of HAp deposition across the surface compared to AK-Zn1, and AK-Zn2. The compressive strength of the zinc-doped akermanite ceramics ranged from 149 to 189 MPa, comparable to that of human cortical bone. Antibacterial and antifungal properties observed in these ceramic powders are essential for preventing infections in orthopedic applications. Additionally, the anti-inflammatory and hemolytic properties reduce inflammation during implantation, providing further benefits. In vitro cytotoxicity studies on Zn-doped akermanite bioceramics (AK-Zn1, AK-Zn2, AK-Zn3) using MG63 cells demonstrated dose-dependent effects, with IC_{50} values of 59.41, 48.47, and 38.26 μg/mL, respectively. Increased Zn levels, as in AK-Zn3, corresponded to higher cytotoxicity. Thus, zinc's role in implanted materials has gained considerable interest, promoting its to its integration into biomaterials designed for implantation requirements. This study suggests that AK-Zn1 is a promising candidate, highlighting the potential of Zn-doped akermanite as a biomaterial for hard tissue engineering applications.

AUTHOR INFORMATION

Corresponding Author

Sasikumar Swamiappan − *Department of Chemistry, School of Advanced Sciences, Vellore Institute of Technology, Vellore 632014 Tamil Nadu, India;* orcid.org/0000-0003-2533-4923; Email: ssasikumar@vit.ac.in

Authors

Shobana Kothandam − *Department of Chemistry, School of Advanced Sciences, Vellore Institute of Technology, Vellore 632014 Tamil Nadu, India*

Selvatharani V − *Department of Chemistry, School of Advanced Sciences, Vellore Institute of Technology, Vellore 632014 Tamil Nadu, India*

Naveensubramaniam Vijayakumar − *Department of Chemistry, School of Advanced Sciences, Vellore Institute of Technology, Vellore 632014 Tamil Nadu, India*

Raveena Ann Alex − *Microbial Biotechnology Laboratory, School of Bio-Sciences and Technology, VIT University, Vellore 632014 Tamil Nadu, India*

Jayanthi Abraham − *Microbial Biotechnology Laboratory, School of Bio-Sciences and Technology, VIT University, Vellore 632014 Tamil Nadu, India*

Selvarasu Maheshwaran − *Department of Materials Engineering, Ming Chi University of Technology, New Taipei City 243303, Taiwan*

Complete contact information is available at: https://pubs.acs.org/10.1021/acsomega.4c05482

Notes

The authors declare no competing financial interest.

REFERENCES

(1) Ono, T.; Nakashima, T. Oral bone biology. *J. Oral Biosci.* **2022**, *64* (1), 8−17.

(2) Reifenrath, J.; Angrisani, N.; Lalk, M.; Besdo, S. Replacement, refinement, and reduction: necessity of standardization and computational models for long bone fracture repair in animals. *J. Biomed. Mater. Res., Part A* **2014**, *102* (8), 2884−2900.

(3) Vallet-Regí, M. Evolution of bioceramics within the field of biomaterials. *C. R. Chim.* **2010**, *13* (1−2), 174−185.

(4) Gandolfi, M. G.; Ciapetti, G.; Taddei, P.; Perut, F.; Tinti, A.; Cardoso, M. V.; Van Meerbeek, B.; Prati, C. Apatite formation on bioactive calcium-silicate cements for dentistry affects surface topography and human marrow stromal cells proliferation. *Dent. Mater.* **2010**, *26* (10), 974−992.

(5) Hughes, E.; Yanni, T.; Jamshidi, P.; Grover, L. M. Inorganic cements for biomedical application: calcium phosphate, calcium sulphate and calcium silicate. *Adv. Appl. Ceram.* **2015**, *114* (2), 65−76.

(6) Bavya Devi, K.; Nandi, S. K.; Roy, M. Magnesium silicate bioceramics for bone regeneration: a review. *J. Indian Inst. Sci.* **2019**, *99*, 261−288.

(7) Wu, C.; Chang, J.; Ni, S.; Wang, J. *In vitro* bioactivity of akermanite ceramics. *J. Biomed. Mater. Res., Part A* **2006**, *76* (1), 73−80.

(8) Hench, L. L. The future of bioactive ceramics. *J. Mater. Sci.: Mater. Med.* **2015**, *26* (2), 86.

(9) Dorozhkin, S. V. Current state of bioceramics. *J. Ceram. Sci. Technol.* **2018**, *9* (4), 353.

(10) Pei, P.; Qi, X.; Du, X.; Zhu, M.; Zhao, S.; Zhu, Y. Three-dimensional printing of tricalcium silicate/mesoporous bioactive glass cement scaffolds for bone regeneration. *J. Mater. Chem. B* **2016**, *4* (46), 7452−7463.

(11) Wu, T.; Lu, T.; Shi, H.; Wang, J.; Ye, J. Enhanced osteogenesis, angiogenesis and inhibited osteoclastogenesis of a calcium phosphate cement incorporated with strontium doped calcium silicate bioceramic. *Ceram. Int.* **2023**, *49* (4), 6630−6645.

(12) Lysenko, O.; Dubok, O.; Borysenko, A.; Shinkaruk, O. The biological properties of the silver-and copper-doped ceramic biomaterial. *J. Nanopart. Res.* **2015**, *17*, 178.

(13) Shao, H.; Zhang, T.; Gong, Y.; He, Y. Silver-containing Biomaterials for Biomedical Hard Tissue Implants. *Adv. Healthcare Mater.* **2023**, *12*, 2300932.

(14) Prameela, P.; Ramya, J. R.; Gajendiran, J.; Gnanam, S.; Ramachandran, K.; Raj, S. G.; Kumar, G. R. Structural, magnetic, and antibacterial activity of the pure, Zn-doped, and Zn-doped/sugar-assisted coprecipitation synthesized semicrystalline Co_3O_4 compound. *J. Mol. Struct.* **2023**, *1292*, 136154.

(15) Samad, N.; Sodunke, T. E.; Abubakar, A. R.; Jahan, I.; Sharma, P.; Islam, S.; Dutta, S.; Haque, M. The implications of zinc therapy in combating the COVID-19 global pandemic. *J. Inflammation Res.* **2021**, *14*, 527−550.

(16) Cacciotti, I. Cationic and anionic substitutions in hydroxyapatite. In *Handbook of bioceramics and biocomposites*, 2016; pp 145−211.

(17) O'Connor, J. P.; Kanjilal, D.; Teitelbaum, M.; Lin, S. S.; Cottrell, J. A. Zinc as a therapeutic agent in bone regeneration. *Materials* **2020**, *13* (10), 2211.

https://doi.org/10.1021/acsomega.4c05482
ACS Omega 2025, 10, 1911−1926

(18) Bhattacharjee, P.; Begam, H.; Chanda, A.; Nandi, S. K. Animal trial on zinc doped hydroxyapatite: A case study. *J. Asian Ceram. Soc.* **2014**, *2* (1), 44−51.
(19) Ullah, I.; Siddiqui, M. A.; Kolawole, S. K.; Liu, H.; Zhang, J.; Ren, L.; Yang, K. Synthesis, characterization and *in vitro* evaluation of zinc and strontium binary doped hydroxyapatite for biomedical application. *Ceram. Int.* **2020**, *46* (10), 14448−14459.
(20) Maleki-Ghaleh, H.; Siadati, M. H.; Fallah, A.; Koc, B.; Kavanlouei, M.; Khademi-Azandehi, P.; Moradpur-Tari, E.; Omidi, Y.; Barar, J.; Beygi-Khosrowshahi, Y.; et al. Antibacterial and cellular behaviors of novel zinc-doped hydroxyapatite/graphene nanocomposite for bone tissue engineering. *Int. J. Mol. Sci.* **2021**, *22* (17), 9564.
(21) Schatkoski, V. M.; do Amaral Montanheiro, T. L.; de Menezes, B. R. C.; Pereira, R. M.; Rodrigues, K. F.; Ribas, R. G.; Thim, G. P. Current advances concerning the most cited metal ions doped bioceramics and silicate-based bioactive glasses for bone tissue engineering. *Ceram. Int.* **2021**, *47* (3), 2999−3012.
(22) Ito, A.; Ojima, K.; Naito, H.; Ichinose, N.; Tateishi, T. Preparation, solubility, and cytocompatibility of zinc-releasing calcium phosphate ceramics. *J. Biomed. Mater. Res., Part A* **2000**, *50* (2), 178−183.
(23) Bootchanont, A.; Wechprasit, T.; Isran, N.; Theangsunthorn, J.; Chaosuan, N.; Chanlek, N.; Kidkhunthod, P.; Yimnirun, R.; Jiamprasertboon, A.; Eknapakul, T.; et al. Correlation of the antibacterial activity and local structure in Zn-and Mn-doped hydroxyapatites by Rietveld refinement and the first-principles method. *Materialia* **2022**, *26*, 101586.
(24) Wu, C.; Chang, J.; Zhai, W.; Ni, S.; Wang, J. Porous akermanite scaffolds for bone tissue engineering: preparation, characterization, and in vitro studies. *J. Biomed. Mater. Res., Part B* **2006**, *78* (1), 47−55.
(25) (a) Punj, S.; Singh, J.; Singh, K. J. C. I. Ceramic biomaterials: Properties, state of the art and future prospectives. *Ceram. Int.* **2021**, *47* (20), 28059−28074. (b) Danks, A. E.; Hall, S. R.; Schnepp, Z. J. M. H. The evolution of 'sol−gel'chemistry as a technique for materials synthesis. *Mater. Horiz.* **2016**, *3* (2), 91−112.
(26) Predoi, D.; Iconaru, S. L.; Predoi, M. V.; Buton, N.; Motelica-Heino, M. Zinc doped hydroxyapatite thin films prepared by sol−gel spin coating procedure. *Coatings* **2019**, *9* (3), 156.
(27) Nigam, A.; Pawar, S. J. Structural, magnetic, and antimicrobial properties of zinc doped magnesium ferrite for drug delivery applications. *Ceram. Int.* **2020**, *46* (4), 4058−4064.
(28) Neščáková, Z.; Zheng, K.; Liverani, L.; Nawaz, Q.; Galusková, D.; Kaňková, H.; Michálek, M.; Galusek, D.; Boccaccini, A. R. Multifunctional zinc ion doped sol−gel derived mesoporous bioactive glass nanoparticles for biomedical applications. *Bioact. Mater.* **2019**, *4*, 312−321.
(29) Bigham, A.; Salehi, A. O. M.; Rafienia, M.; Salamat, M. R.; Rahmati, S.; Raucci, M. G.; Ambrosio, L. Zn-substituted Mg2SiO4 nanoparticles-incorporated PCL-silk fibroin composite scaffold: A multifunctional platform towards bone tissue regeneration. *Mater. Sci. Eng. C* **2021**, *127*, 112242.
(30) Mahanty, A.; Shikha, D. Design of a new Ag/Mg/Zn alloyed doped hydroxyapatite hybrid biomaterial. *Mater. Chem. Phys.* **2024**, *311*, 128553.
(31) Mahanty, A.; Shikha, D. Design of a new Ag/Mg/Zn alloyed doped hydroxyapatite hybrid biomaterial. *Mater. Chem. Phys.* **2024**, *311*, 128553.
(32) Choudhary, R.; Manohar, P.; Vecstaudza, J.; Yáñez-Gascón, M. J.; Sánchez, H. P.; Nachimuthu, R.; Locs, J.; Swamiappan, S. Preparation of nanocrystalline forsterite by combustion of different fuels and their comparative in-vitro bioactivity, dissolution behaviour and antibacterial studies. *Mater. Sci. Eng. C* **2017**, *77*, 811−822.
(33) Choudhary, R.; Venkatraman, S. K.; Chatterjee, A.; Vecstaudza, J.; Yáñez-Gascón, M. J.; Perez-Sanchez, H.; Locs, J.; Abraham, J.; Swamiappan, S. Biomineralization, antibacterial activity and mechanical properties of biowaste derived diopside nanopowders. *Adv. Powder Technol.* **2019**, *30* (9), 1950−1964.
(34) Vijayakumar, N.; Venkatraman, S. K.; Nandakumar, R.; Alex, R. A.; Abraham, J.; Mohammadi, H.; Ebadi, M.; Swamiappan, S. Optimization of Metal Ion/Fuel Ratio for an Effective Combustion of Monticellite and Investigation of Its Microbial and Hemolytic Activity for Biomedical Applications. *ACS omega* **2023**, *8* (40), 36919−36932.
(35) Collin, S. M.; Augustine, J.; Abraham, J.; Sasikumar, S. Thermo-mechanical stability and antibacterial activity of merwinite derived from different fuels. *J. Mater. Res.* **2023**, *38* (23), 5045−5054.
(36) Joseph, S.; Swamiappan, S. Enhancement of Bioactivity, Mechanical and Degradation Properties of the Diopside by Incorporation of Ba^{2+} Ion via Sol−gel Combustion Route. *Silicon* **2024**, *16*, 6241−6255.
(37) Huang, Y.; Zhang, H.; Qiao, H.; Nian, X.; Zhang, X.; Wang, W.; Zhang, X.; Chang, X.; Han, S.; Pang, X. Anticorrosive effects and *in vitro* cytocompatibility of calcium silicate/zinc-doped hydroxyapatite composite coatings on titanium. *Appl. Surf. Sci.* **2015**, *357*, 1776−1784.
(38) Wu, C.; Chang, J. Synthesis and apatite-formation ability of akermanite. *Mater. Lett.* **2004**, *58* (19), 2415−2417.
(39) Gomes, S.; Nedelec, J. M.; Jallot, E.; Sheptyakov, D.; Renaudin, G. Unexpected mechanism of Zn2+ insertion in calcium phosphate bioceramics. *Chem. Mater.* **2011**, *23* (12), 3072−3085.
(40) Sagadevan, S.; Pal, K.; Chowdhury, Z. Z.; Hoque, M. E. Structural, dielectric and optical investigation of chemically synthesized Ag-doped ZnO nanoparticles composites. *J. Sol-Gel Sci. Technol.* **2017**, *83*, 394−404.
(41) Black, L.; Garbev, K.; Stemmermann, P.; Hallam, K. R.; Allen, G. C. Characterisation of crystalline CSH phases by X-ray photoelectron spectroscopy. *Cem. Concr. Res.* **2003**, *33* (6), 899−911.
(42) Gomes, S.; Vichery, C.; Descamps, S.; Martinez, H.; Kaur, A.; Jacobs, A.; Nedelec, J. M.; Renaudin, G. Cu-doping of calcium phosphate bioceramics: From mechanism to the control of cytotoxicity. *Acta Biomater.* **2018**, *65*, 462−474.
(43) Banerjee, D.; Sudarsan, V.; Wattal, P. K.; Das, D. The effect of divalent cation modifiers on the physicochemical properties of borosilicate glasses with high Cs contents. *Phys. Chem. Glas.: Eur. J. Glass Sci.* **2013**, *54* (4), 157−163.
(44) Shang, S.; Zhao, Q.; Zhang, D.; Sun, R.; Tang, Y. Molecular dynamics simulation of the adsorption behavior of two different drugs on hydroxyapatite and Zn-doped hydroxyapatite. *Mater. Sci. Eng. C* **2019**, *105*, 110017.
(45) Lv, J.; Zhang, S.; Wang, S.; Luo, L.; Huang, H.; Zhang, J. Chemical transformation of zinc oxide nanoparticles as a result of interaction with hydroxyapatite. *Colloids Surf., A* **2014**, *461*, 126−132.
(46) Choudhary, R.; Vecstaudza, J.; Krishnamurithy, G.; Raghavendran, H. R. B.; Murali, M. R.; Kamarul, T.; Swamiappan, S.; Locs, J. In-vitro bioactivity, biocompatibility and dissolution studies of diopside prepared from biowaste by using sol−gel combustion method. *Mater. Sci. Eng. C* **2016**, *68*, 89−100.
(47) Kharaziha, M.; Fathi, M. H. Synthesis and characterization of bioactive forsterite nanopowder. *Ceram. Int.* **2009**, *35* (6), 2449−2454.
(48) Liu, A.; Sun, M.; Yang, X.; Ma, C.; Liu, Y.; Yang, X.; Yan, S.; Gou, Z. Three-dimensional printing akermanite porous scaffolds for load-bearing bone defect repair: An investigation of osteogenic capability and mechanical evolution. *J. Biomater. Appl.* **2016**, *31* (5), 650−660.
(49) Mohammadi, M.; Tulliani, J. M.; Montanaro, L.; Palmero, P. Gelcasting and sintering of hydroxyapatite materials: Effect of particle size and Ca/P ratio on microstructural, mechanical and biological properties. *J. Eur. Ceram. Soc.* **2021**, *41* (14), 7301−7310.
(50) Baino, F.; Yamaguchi, S. The use of simulated body fluid (SBF) for assessing materials bioactivity in the context of tissue engineering: review and challenges. *Biomimetics* **2020**, *5* (4), 57.
(51) Li, P.; Dai, J.; Li, Y.; Alexander, D.; Čapek, J.; Geis-Gerstorfer, J.; Wan, G.; Han, J.; Yu, Z.; Li, A. Zinc based biodegradable metals for bone repair and regeneration: Bioactivity and molecular mechanisms. *Materials Today Bio* **2023**, *25*, 100932.

https://doi.org/10.1021/acsomega.4c05482
ACS Omega 2025, 10, 1911−1926

(52) Igathinathane, C.; Tumuluru, J. S.; Sokhansanj, S.; Bi, X.; Lim, C. J.; Melin, S.; Mohammad, E. Simple and inexpensive method of wood pellets macro-porosity measurement. *Bioresour. Technol.* **2010**, *101* (16), 6528−6537.
(53) Applerot, G.; Lipovsky, A.; Dror, R.; Perkas, N.; Nitzan, Y.; Lubart, R.; Gedanken, A. Enhanced antibacterial activity of nanocrystalline ZnO due to increased ROS-mediated cell injury. *Adv. Funct. Mater.* **2009**, *19* (6), 842−852.
(54) Jin, G.; Cao, H.; Qiao, Y.; Meng, F.; Zhu, H.; Liu, X. Osteogenic activity and antibacterial effect of zinc ion implanted titanium. *Colloids Surf., B* **2014**, *117*, 158−165.
(55) Tuon, F. F.; Suss, P. H.; Telles, J. P.; Dantas, L. R.; Borges, N. H.; Ribeiro, V. S. T. Antimicrobial treatment of Staphylococcus aureus biofilms. *Antibiotics* **2023**, *12* (1), 87.
(56) Li, Y.; Yang, Y.; Qing, Y. A.; Li, R.; Tang, X.; Guo, D.; Qin, Y. Enhancing ZnO-NP antibacterial and osteogenesis properties in orthopedic applications: a review. *Int. J. Nanomed.* **2020**, *15*, 6247−6262.
(57) Huzum, B.; Puha, B.; Necoara, R. M.; Gheorghevici, S.; Puha, G.; Filip, A.; Alexa, O. Biocompatibility assessment of biomaterials used in orthopedic devices: An overview. *Exp. Ther. Med.* **2021**, *22* (5), 1315.
(58) Khan, M.; Naqvi, A. H.; Ahmad, M. Comparative study of the cytotoxic and genotoxic potentials of zinc oxide and titanium dioxide nanoparticles. *Toxicology reports* **2015**, *2*, 765−774.
(59) Gammoh, N. Z.; Rink, L. Zinc in infection and inflammation. *Nutrients* **2017**, *9* (6), 624.
(60) Velard, F.; Laurent-Maquin, D.; Braux, J.; Guillaume, C.; Bouthors, S.; Jallot, E.; Nedelec, J. M.; Belaaouaj, A.; Laquerriere, P. The effect of zinc on hydroxyapatite-mediated activation of human polymorphonuclear neutrophils and bone implant-associated acute inflammation. *Biomaterials* **2010**, *31* (8), 2001−2009.
(61) Vijayakumar, N.; Swamiappan, S. Investigation on the Synthesis, Biomineralization, Mechanical Strength and Biocompatibility of Rankinite Bioceramics Derived from Eggshell and Rice Husk Waste for Biomedical Applications. *ChemistrySelect* **2023**, *8* (44), No. e202302984.
(62) Lv, Y.; Song, X.; Lei, T.; Yin, P. Structural and antibacterial properties of doped zinc oxide and their composites with hydroxyapatite. *Colloids Surf., A* **2022**, *651*, 129706.

https://doi.org/10.1021/acsomega.4c05482
ACS Omega 2025, 10, 1911−1926